ORIGINAL ARTICLE

Multi-scale ionosphere responses to the May 2017 magnetic storm over the Asian sector

Lei Liu[1,2] · Shasha Zou[2] · Yibin Yao[1] · Ercha Aa[2]

Abstract

We investigate multi-scale ionospheric responses to the May 27, 2017, geomagnetic storm over the Asian sector by using multi-instrumental observations, including ground-based global navigation satellite systems (GNSS) network, constellation observing system for meteorology, ionosphere and climate radio occultation, the FengYun-3C (FY-3C) GNSS occultation sounder electron density profiles and in situ plasma density observations provided by both Swarm and defense meteorological satellite program missions. This geomagnetic storm was an intense storm with the minimum symmetric horizontal component reaching − 150 nT and was caused by a coronal mass ejection released on May 23. The main observations are summarized below: (1) two ionospheric positive storm periods were observed. The first one was observed in the noon–afternoon sector during the main phase of the storm on May 28, with nearly 120% TEC enhancement. The second one was of a smaller scale and occurred on the nightside during the recovery phase of the storm on May 29. The first dayside positive storm was initiated by the interplanetary magnetic field (IMF) Bz southward turning and eastward penetration electric field, while the second nightside one was terminated by a later southward turning of the IMF Bz since the Asian sector was on the nightside and the penetration electric field changed westward. (2) A negative storm occurred from 00:00 to 12:00 UT on May 30 over the Asian sector, nearly 2 days after the main phase, which was due to the thermospheric composition change, i.e., decrease in the O/N_2 ratio, as shown in the TIMED/GUVI measurements. (3) A band-like TEC enhancement was observed aligning in the northwest–southeast direction and propagated slowly southwestward from 15:00 to 20:00 UT (23:00–04:00 LT, near midnight) on May 28 during the recovery phase of the storm. In situ density observations from the Swarm B and DMSP F15&16 satellites confirmed the density enhancement at 510 km and 850 km, respectively, and revealed that this band-like TEC enhancement structure resembles the so-called plasma blob. The similarities of the observed plasma blob characteristics in terms of spatial structure, propagation trend and temporal evolution with the nighttime traveling ionospheric disturbance (TID) are consistent with the TID-blob theory.

Keywords Positive and negative ionosphere responses · Blob structure · TID · Geomagnetic storm

Introduction

The enhanced solar wind energy enters the magnetosphere–ionosphere–thermosphere system suddenly during a geomagnetic storm, and as a result, various features in ionospheric electron density occur. In the last decade, the integrated ionospheric electron density or total electron content (TEC) derived from various global navigation satellite systems (GNSS) has been increasingly used in sensing the ionospheric responses to space weather disturbances in addition to the original positioning, navigation and timing (PNT) service. Ionospheric TEC structures with various spatial and temporal scales have been revealed by regional and continental scale TEC maps. Understanding the formation and

✉ Lei Liu
  leiliu@whu.edu.cn

1 School of Geodesy and Geomatics, Wuhan University, Wuhan, China

2 Department of Climate and Space Sciences and Engineering, University of Michigan, Ann Arbor, MI, USA

development of these structures is of practical importance since these structures often possess density gradients, where ionospheric irregularities and thus disruptions of GNSS service tend to occur.

The mid-low latitude large-scale decrease and increase in electron densities/TEC during the storm time are usually referred to as negative and positive ionospheric storms, respectively. Negative ionospheric storm effects have primarily been related to thermospheric composition changes (Fuller-Rowell et al. 1994), while understanding the generation and evolution of positive ionospheric storms remains difficult due to complex and competing physical mechanisms, such as storm time equatorward thermospheric winds, prompt penetration electric fields (PPEF), disturbance dynamo electric fields (DDEF) and traveling atmospheric disturbances (TAD) or a combination of them (Huang et al. 2005; Crowley et al. 2006; Danilov 2013; Mendillo 2006). A number of storms have attracted much attention, such as in October 2003 (Mannucci et al. 2005; Abdu et al. 2007), March 2015 (Astafyeva et al. 2015; Nava et al. 2016) and June 2015 (Astafyeva et al. 2017, 2018; Singh and Sripathi 2017).

The PPEF is primarily related to the IMF Bz direction and the evolution of the equatorial ring current shielding effect. The dayside PPEF (under-shielding condition) is eastward after the southward turning of the IMF Bz, while it is westward on the nightside. During over-shielding conditions, i.e., either after rapid IMF Bz northward turning or substorm injection, the PPEF directions reverse. In contrast to the PPEF, the DDEF takes time to develop, usually longer than 3 h, and varies slowly with time; its direction is westward on the dayside but eastward on the nightside, which is opposite to the PPEF. Moreover, besides the dynamo effect, neutral winds can directly affect the dynamic structures of the mid-low latitude ionosphere through ion-neutral collisions. In general, eastward electric field and/or equatorward neutral wind will uplift the F layer in the mid-low latitude regions to higher altitudes where the recombination process is slower and hence increase the electron densities/TEC, whereas westward electric field and/or poleward neutral wind will lower the F layer to lower altitudes where the recombination process is faster and result in the decline of electron densities/TEC significantly (Mendillo 2006; Lu et al. 2008, 2012; Zou et al. 2013, 2014).

Apart from the above-mentioned large-scale ionospheric features, such as positive and negative ionospheric effects during geomagnetic storms, mesoscale dynamical structures have also been observed in the middle and low latitudes. In general, plasma bubbles, plasma blobs and medium-scale traveling ionospheric disturbances (MSTIDs) are the three major mesoscale ionosphere structures. Plasma bubbles are deep density depletions, which are caused by the generalized Rayleigh–Taylor (R–T) instability after sunset (Abdu 2012; Abadi et al. 2015; Cherniak and Zakharenkova 2016; Aa et al. 2018). Plasma blobs are plasma density enhancements relative to the background ionosphere, and they have usually been observed in the $\pm(20°–30°)$ magnetic latitude regions on the nightside (Park et al. 2003; Furno et al. 2008; Huang et al. 2014; Miller et al. 2014). Nighttime MSTIDs are typically wave-like structures in the ionosphere with horizontal wavelengths of several hundred kilometers and propagation speed of 50–250 m/s. (Garcia et al. 2000; Saito et al. 2001; Otsuka et al. 2004; Tsugawa et al. 2007).

These three mesoscale structures could be inter-related. For example, the nighttime plasma blobs have been suggested to be related to equatorial plasma bubbles (Park et al. 2003; Le et al. 2003; Furno et al. 2008; Huang et al. 2014). Park et al. (2003) reported plasma blob events in the low-latitude F region by using the plasma density data measured by the KOMPSAT-1 and DMSP F15 satellites. They found that the characteristics of the plasma blobs were similar to those of the equatorial plasma bubbles, so it is suggested that the blobs originated from the lower altitudes by a mechanism that drives an upward drift of the plasma bubbles. Huang et al. (2014) found that plasma blobs can occur during various stages of bubble evolution and proposed a scenario to explain their relationship. However, some blob structures are observed when plasma bubbles are absent, so bubbles may not be a necessary condition for the development of blobs (Kil et al. 2011, 2015; Haaser et al. 2012; Choi et al. 2012; Kil and Paxton 2017). In recent years, the plasma blobs are also suggested to be associated with the nighttime MSTIDs (Choi et al. 2012; Miller et al. 2014; Kil and Paxto 2017; Kil et al. 2019). For example, Miller et al. (2014) reported that MSTIDs were observed at the same time as plasma blobs observed by the C/NOFS satellite. This MSTID-blob connection can be well explained by a modulation of the O+ profile altitude due to electric fields within the MSTID. Kil et al. (2019) reported four blob events by using the Swarm satellite in situ electron, and those observed blobs aligned in the northwest–southeast direction in the northern hemisphere and southwest–northeast direction in the southern hemisphere, which are typical characteristics of nighttime MSTIDs.

An intense geomagnetic storm occurred on May 27, 2017, and complicated multi-scale ionosphere structures occurred during this storm. In this work, both large-scale (positive and negative storms) and mesoscale (nighttime band-like TEC enhancement) ionospheric responses to this storm over the Asian sector are investigated by using multi-instrumental observations.

Data and methodology

To study the ionospheric responses to the May 2017 geomagnetic storm over the Asian sector, we used multi-instrumental observations, including ground-based GNSS network, COSMIC RO and FY-3C GNSS GNOS electron density profiles, as well as in situ plasma densities provided by both Swarm and DMSP missions.

GNSS TEC and relevant datasets

About 270 ground-based dual-frequency GNSS receivers, provided by the Crustal Movement Observation Network of China (CMONOC) and International GNSS Service (IGS) network, are used to investigate regional ionospheric responses to this geomagnetic storm. Figure 1 shows the distribution of the GNSS receivers in geographic coordinates with magnetic latitudes highlighted by magenta lines. The GNSS data used in this study are typically sampled every 30 s, and the cutoff elevation angle used is 25°, in order to remove multipath effects.

The ionospheric absolute slant TEC (STEC) from satellite to each receiver is derived by the carrier-smoothing-code algorithm (Jin et al. 2012; Yao et al. 2018) after the differential code biases (DCB) from both satellites and receivers have been removed. The STEC is then converted to vertical TEC (VTEC, hereafter referred as TEC for simplification) by using a thin shell model assuming an ionospheric pierce point (IPP) height of 300 km, which is selected after taking into consideration of the hmF2 data from ionosonde and Constellation Observing System for Meteorology,
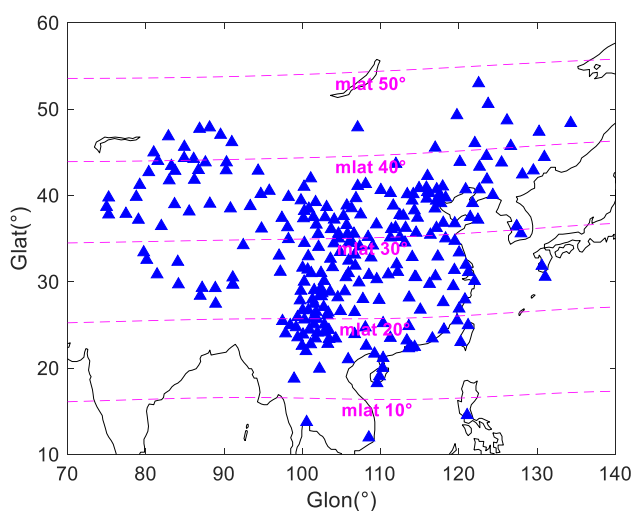
Ionosphere and Climate (COSMIC) over the Asian sector during this storm. Finally, the two-dimensional (2D) TEC map is obtained by averaging all available IPP TEC values into cells of 1° latitude and 1° longitude within a 15-min sliding window, and no spatial interpolation procedure is used to generate these maps. To detect wave-like features in TEC, such as TID, we remove the background variations for each continuous TEC arc by using the cubic polynomial fitting. Then, the detrended TEC time series for each visible receiver–satellite pair is the residual after subtracting the fitted curve from the observed TEC values. The 2D detrended TEC maps are constructed in a similar way to the above-mentioned 2D TEC maps.

For monitoring ionospheric irregularities and phase fluctuations, rate of TEC (ROT) changes and its 5-min standard deviation (ROTI) are also calculated (Pi et al. 1997; Yao et al. 2016; Cherniak et al. 2018), which is a standard method to represent sharp density gradients in time series. In order to specify the spatial distribution of ionospheric irregularities and fluctuations over the Asian sector, the 2D ROTI maps are constructed for all available satellite–receiver ray paths with the same spatial resolution 1×1 every 15 min.

Ionospheric densities measured by other instruments

To observe the ionospheric electron density variations at different altitudes, the electron density profiles (EDP) obtained from both the COSMIC Radio Occultation (RO) and the FengYun-3C (FY-3C) GNSS Occultation Sounder (GNOS) missions are used in this study. There were six COSMIC satellites operating in six circular orbits with 72° inclination angle at 800 km, but currently, only one COSMIC satellite works normally. Here, the inverted EDPs from this satellite are used to study the altitude variations of the electron density within the targeted area. Moreover, EDPs from FY-3C GNOS are also used in this study, which are provided by the National Satellite Meteorological Center, China. FY-3C, designed to track both GPS and BDS signals, is a low-earth-orbit (LEO) satellite with an altitude of 836 km and inclination of 98.75°, launched in September 2013. In situ electron density (Ne) data from the Swarm B satellite at 510 km, and DMSP F15&F16 at 835 km are also used in this study.

TIMED GUVI O/N$_2$ ratio

The ratio of column-integrated atomic oxygen number density to molecular nitrogen number density (O/N$_2$ ratio) in the thermosphere provided by the Thermosphere Ionosphere Mesosphere Energetics and Dynamics (TIMED) Global Ultraviolet Imager (GUVI) is employed in this study to provide us the storm-time thermosphere composition variations. The TIMED/GUVI satellite, flying at a 630 km circular orbit

Fig. 1 GNSS receiver locations over China and adjacent areas. Magenta dashed curves represent magnetic latitudes (mlat). Glat and Glon refer to geographic latitude and longitude, respectively

and a 74.1° inclination, can scan a view of a 2000-km-wide swath along its orbit (Christensen et al. 2003).

Interplanetary and geomagnetic conditions of May 25–30

An intense geomagnetic storm caused by a corona mass ejection (CME), occurred on May 27, 2017. From top to bottom, Fig. 2 shows the temporal evolution of auroral electrojet index (AE), Kp, solar wind velocity and dynamic pressure (Vsw and Psw), interplanetary magnetic field (IMF) Bz component and the SYM-H index. The earth-directed CME was launched on May 23, 2017, and reached the earth at 15:30 UT on May 27, 2017, triggering the sudden storm commencement (SSC). At the shock front, the Vsw increased suddenly from 300 to 400 km/s and the dynamic pressure Psw jumped from 1.2 to 15 nPa. The following magnetic cloud with strong southward IMF (< -20 nT) led to a classic development of a geomagnetic storm with the main phase occurring from 21:30 UT on May 27 to 07:10 UT on May 28, and the recovery phase after 07:10 UT on May 28. After the first CME impact, there were two episodes of southward IMF Bz around 12:00 UT on May 29 and early times on May 30, which are also associated with enhanced geomagnetic activities as shown in AE and Kp.
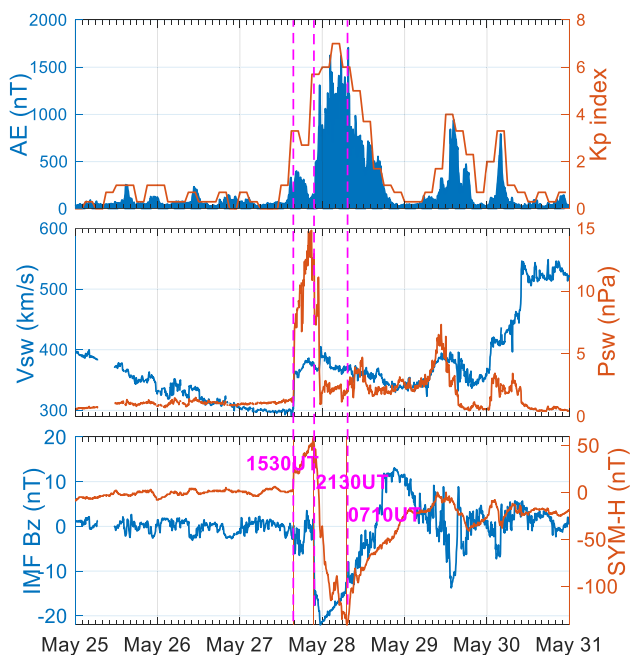
Fig. 2 Variations of geomagnetic conditions during May 25–30, 2017: auroral electrojet (AE), Kp, velocity and dynamic pressure of the solar wind (Vsw and Psw), interplanetary magnetic field (IMF) Bz component and the SYM-H index. Three vertical magenta dashed lines represent the starting time of the SSC, main phase and recovery phase, respectively

The minimum SYM-H reached -150 nT, and thus this storm is classified as an intense geomagnetic storm.

Multi-scale ionosphere responses

Both large-scale (positive and negative storms) and mesoscale (nighttime band-like TEC enhancement) ionospheric features to this storm over the Asian sector are investigated by using multi-instrumental observations.

### Regional positive and negative ionospheric storms

To illustrate the large-scale TEC behavior over the Asian sector, we constructed 2D absolute TEC maps with a 15-min interval, and then the TEC change relative to the quiet-time background condition ($\triangle$TEC (%)) is calculated. Here, the quiet time TEC on May 26 is regarded as the background TEC and removed from the storm time TEC.

Figure 3 shows $\triangle$TEC (%) maps with a two-hour interval in geographic coordinates during the main phase and early recovery phase of the storm between 01:00 and 11:00 UT on May 28, when the Asian sector rotated from the morning to the dusk sector. The TEC began to increase in the north-eastern part of China at 01:00 UT shortly after the IMF Bz southward turning, a signature of a classic positive storm. Then, the positive storm gradually strengthened and extended to the southwest direction to some degree, and the maximum TEC increment reached 120% around 03:00–05:00 UT ($+8$ h $= 11:00$–13:00 LT, Beijing Time) on May 28 between 100°E and 130°E at 35°–45° N. After 07:00 UT on May 28, the TEC enhancement weakened gradually.

In addition to the positive ionospheric storm occurred over Asia on May 28, another positive phase occurred on May 29 when this sector was on the nightside (hereafter, the positive storms observed on May 28 and 29 are referred as the first and second positive storm, respectively). Figure 4 shows this TEC enhancement development during the late recovery phase of the storm between 11:00 and 21:00 UT (19:00–05:00 LT) on May 29, 2017, in a similar form of Fig. 3. From 11:00 UT to 13:00 UT (19:00–21:00 LT) on May 29, a positive storm was observed at 70°E–100°E and strengthened gradually. Then, another TEC enhancement appeared at lower latitudes at approximately 13:00 UT (21:00 LT) on May 29 and extended to relatively high latitudes with maximum increment of more than 100% around 15:00–17:00 UT (23:00–01:00 LT) on May 29. After 19:00 UT, the positive storm started to decay slowly and recovered to normal level until the end of this day (full sets of 2D $\triangle$TEC maps with 15-min intervals are available in Movie 3 of the supporting information).

Figure 5 presents temporal variations of differential TEC (DTEC) for three meridional chains across China (80°E,
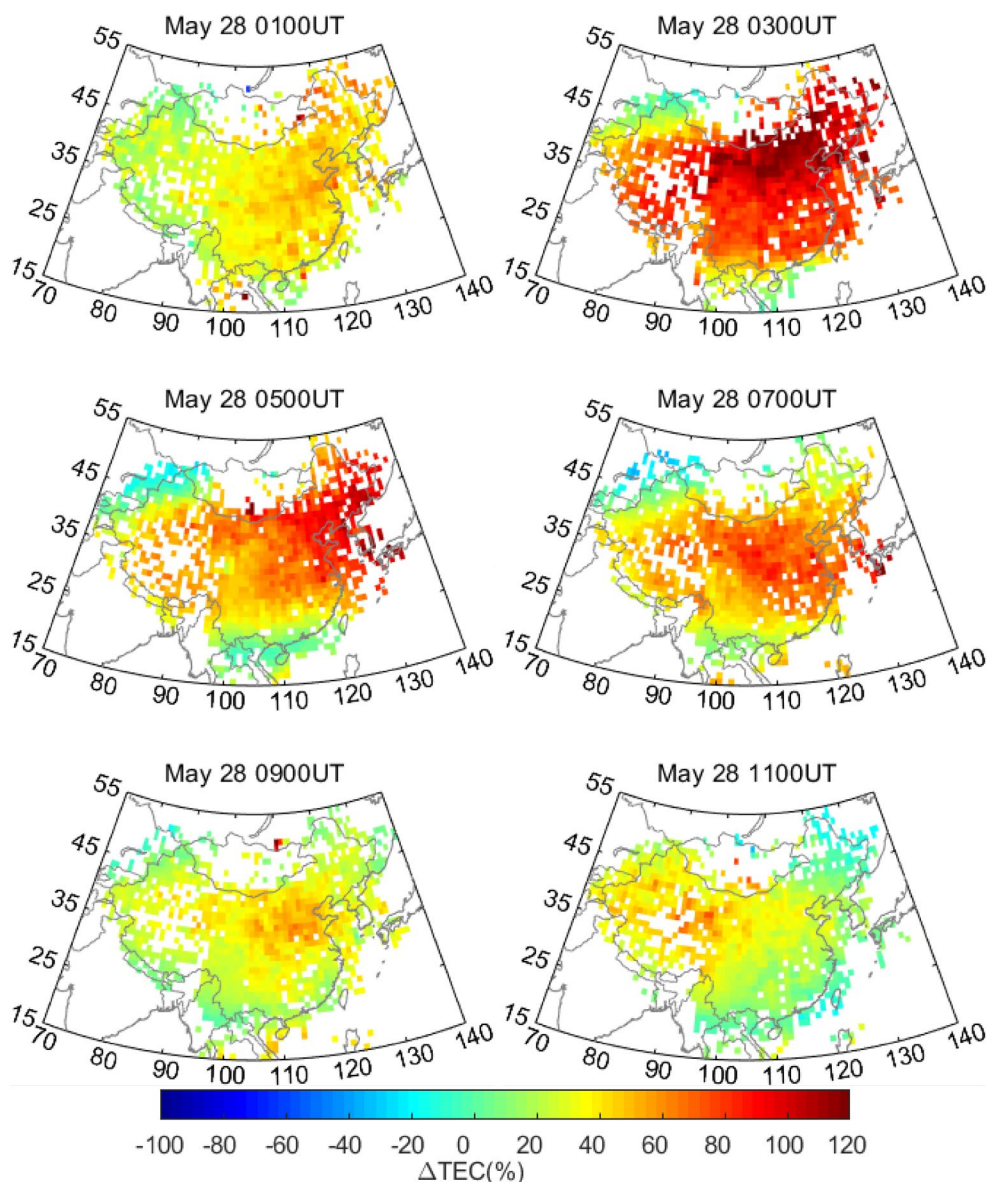
Fig. 3 2D $\triangle$TEC (%) maps with a two-hour interval over the Asian sector from 01:00 to 11:00 UT (09:00–19:00 LT) on May 28. The quiet time TEC on May 26 during this period is regarded as the background TEC and removed from the storm time TEC. 2D abso-lute TEC and $\triangle$TEC (%) maps for 15-min resolution are available in Movies 1 and 2 of the supporting information. Beijing time is regarded as local time (LT), which is converted from universal time (UT) by plus 8 h, namely LT = UT + 8 h

100°E and 120°E). The DTEC from each meridional chain is constructed by selecting TEC data within ± 3° of the central longitude. The averaged TEC value of May 25 and 26 is used as the background TEC and has been subtracted. Compared to the quiet days, two positive storm events mentioned above can be clearly seen on May 28 and 29, respectively. The IMF Bz component is also shown in the right axis for easy comparison.

The first positive storm initiated at approximately 01:00 UT on May 28 over three meridional chains and lasted for over 20 h, with the most intensive enhancement of 20

TECU occurred around 03:00–07:00 UT. This long-lasting positive phase matches well with the duration of the southward IMF Bz within this magnetic cloud. Interestingly, the second positive storm occurred slightly before the second southward turning of IMF Bz and on the nightside. Therefore, these two positive storms could be generated due to different mechanisms and will be further discussed in the discussion section.

In Fig. 5, one can also see significantly reduced TEC at these three longitudes during the first half of May 30, with the most severe TEC decrease reaching about 10 TECU

Fig. 4 2D △TEC (%) maps with a two-hour interval over the Asian sector from 11:00 to 21:00 UT (19:00–05:00 LT) on May 29, 2017. Quiet time TEC on May 26 is regarded as the background value and removed from the storm time TEC
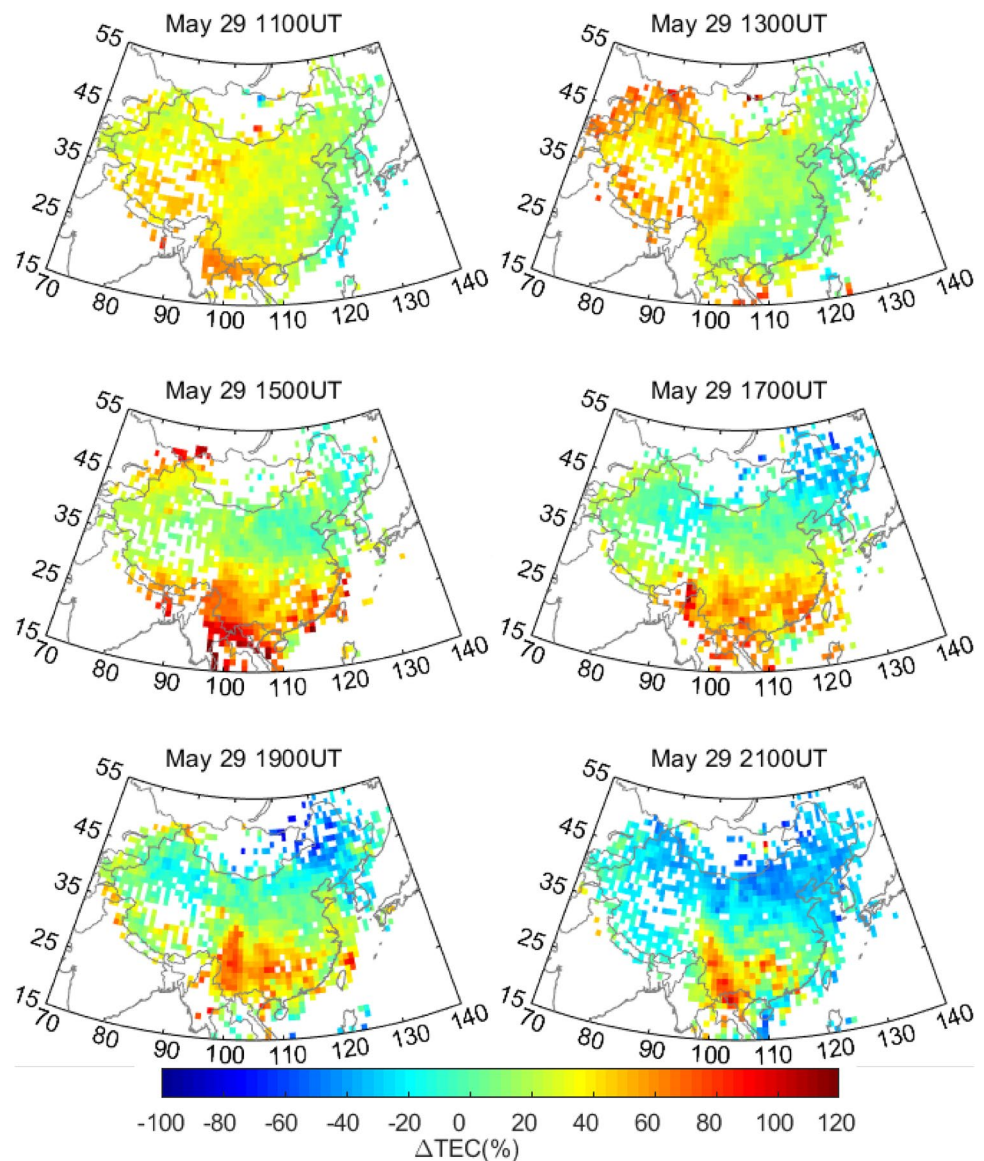
below 30°N at 120°E around 06:00 UT, which is a classic signature of negative ionosphere storm.

## Mesoscale TEC enhancement structure observed near midnight sector

Figure 6 shows 2D TEC maps with a 1-hour interval around 15:00–20:00 UT (23:00–04:00 LT, near midnight) on May 28, i.e., during the rapid recovery phase of the storm. A band-like TEC structure aligned in the northwest–southeast direction started to appear at 120°E and 20–40° geographic latitudes (15–35° magnetic latitudes) at 15:00 UT on May 28 and moved toward southwest with time (see the red slant line in each panel). The drift speed is very slow, close to 90 m/s, which is the average value estimated from every two consecutive TEC maps. This TEC band structure does

not show clear enhancement comparing with the TEC value further to the west of China, but it decreased slower than the surrounding region.

Discussions

In this part, we will discuss the formation mechanisms of the multi-scale ionospheric responses, including two ionospheric positive storms observed in the noon–afternoon sector during the main phase and the nightside during the recovery phase, respectively, one negative storm occurred nearly two days after the main phase, and the band-like TEC enhancement structure occurred near midnight sector during the recovery phase.

Fig. 5 Differential TEC (DTEC) variations as a function of geographic latitude and time at three meridional chains: 80°E (top), 100°E (middle) and 120°E (bottom). Each meridional chain is centered within ±3° in longitude. DTEC is determined by subtracting the background TEC, which is the averaged TEC value on May 25 and 26. Temporal variations of IMF Bz (red curves) are marked in the right axis. Three vertical magenta dashed lines represent the starting time of the SSC, main phase and recovery phase, respectively. LT = UT + 8 h
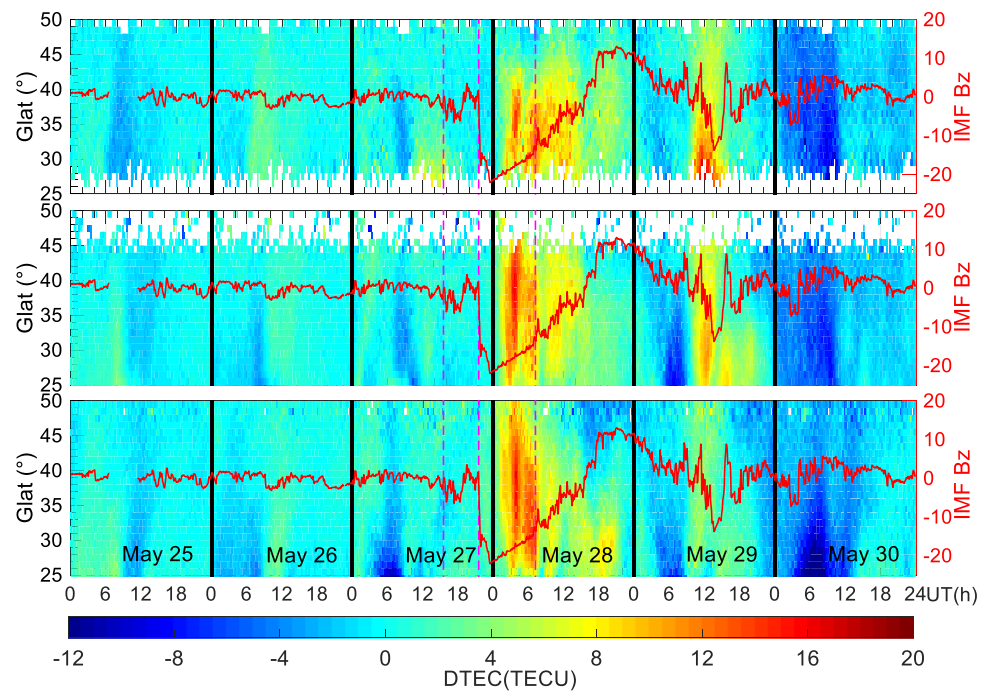
Formation mechanisms of the two positive storms

Two positive storms at mid-low latitudes over the Asian sector were observed by ground-based GNSS TEC maps: the first one was observed on the dayside and lasted for more than 20 h, which is comparable to the duration of the southward IMF Bz within the magnetic cloud; and the second one occurred in the pre-midnight sector and just before the second IMF Bz southward turning. In order to understand the generation mechanisms of these two positive storms, we explore other datasets to reveal their characteristics at various altitudes of the ionosphere and mainly F layer.

Figure 7 shows selected EDPs obtained from both the COSMIC RO and FY-3C GNOS. The storm-time EDPs (red curves) are compared with the quiet-time ones (green curves) at similar UTs/LTs. The locations of the EDPs are shown in geographic coordinates in the upper right corner of each panel. As one can see, the electron density (Ne) during both positive storms exhibited a considerable increase in NmF2, ranging from 50 to 150% increase (see the top and middle row of Fig. 7). The hmF2 during the first positive storm on the dayside increased from 220 to 350 km at 36°N, suggesting that there was a significant ionospheric uplift. Therefore, together with the TEC observations presented in the previous section, the density enhancement during the first positive storm observed by both the COSMIC RO and FY-3C GNOS EDPs suggests that the first positive storm was due to the imbalance between the production and loss resulted from the upward lifting of the F layer (Mendillo 2006; Heelis et al. 2009; Lu et al. 2012; Zou et al. 2013, 2014). Once the F layer is lifted to higher altitudes, the

recombination rate would decrease and reduce the plasma loss rate. At the same time, solar EUV production is still ongoing, leading to an enhancement in the TEC.

As for the physical mechanisms that cause the F layer uplift, it can be due to PPEF and/or equatorward thermospheric wind. Using the TIEGCM model, Lu et al. (2012) found that the PPEF is more important in the dayside subauroral and low-latitude region during the first couple of hours after the Bz southward turning, while the thermospheric wind is more important in the mid-latitude region. Considering that the most significant lift observed is at 36°N and six hours after the southward turning, it is likely that the equatorward thermospheric wind plays a more important role.

The second positive storm was observed when the Asian sector was on the nightside. It initiated slightly before the IMF Bz second southward turning at the end of the storm recovery phase and then rapidly recovered after the second southward turning. This southward turning was weaker than the first one, and the duration was also shorter, so the SYM-H only decreased to −30 nT and thus was not negative enough to enable this storm to be classified as a double-dip storm. On the nightside, the PPEF should be westward and the associated $E \times B$ drift should be downward. Therefore, the second IMF Bz southward turning disrupted the second positive phase suddenly and likely descended the F layer. The peak TEC of the second positive phase also occurred around 20 mlat, lower than the first positive phase and in the range of the typical equatorial ionization anomaly (EIA) crest region. We suggest that the second positive phase is likely part of the nighttime EIA crest and formed due to nighttime eastward DDEF. This nighttime eastward DDEF

Fig. 6 Hourly 2D TEC maps over the Asian sector from 15:00 to 20:00 UT (23:00–04:00 LT) on May 28. Full sets of 2D TEC maps with a 15-min interval are available in Movie 4 of the supporting information. The red slant line in each panel denotes the alignment of the TEC enhancement structure
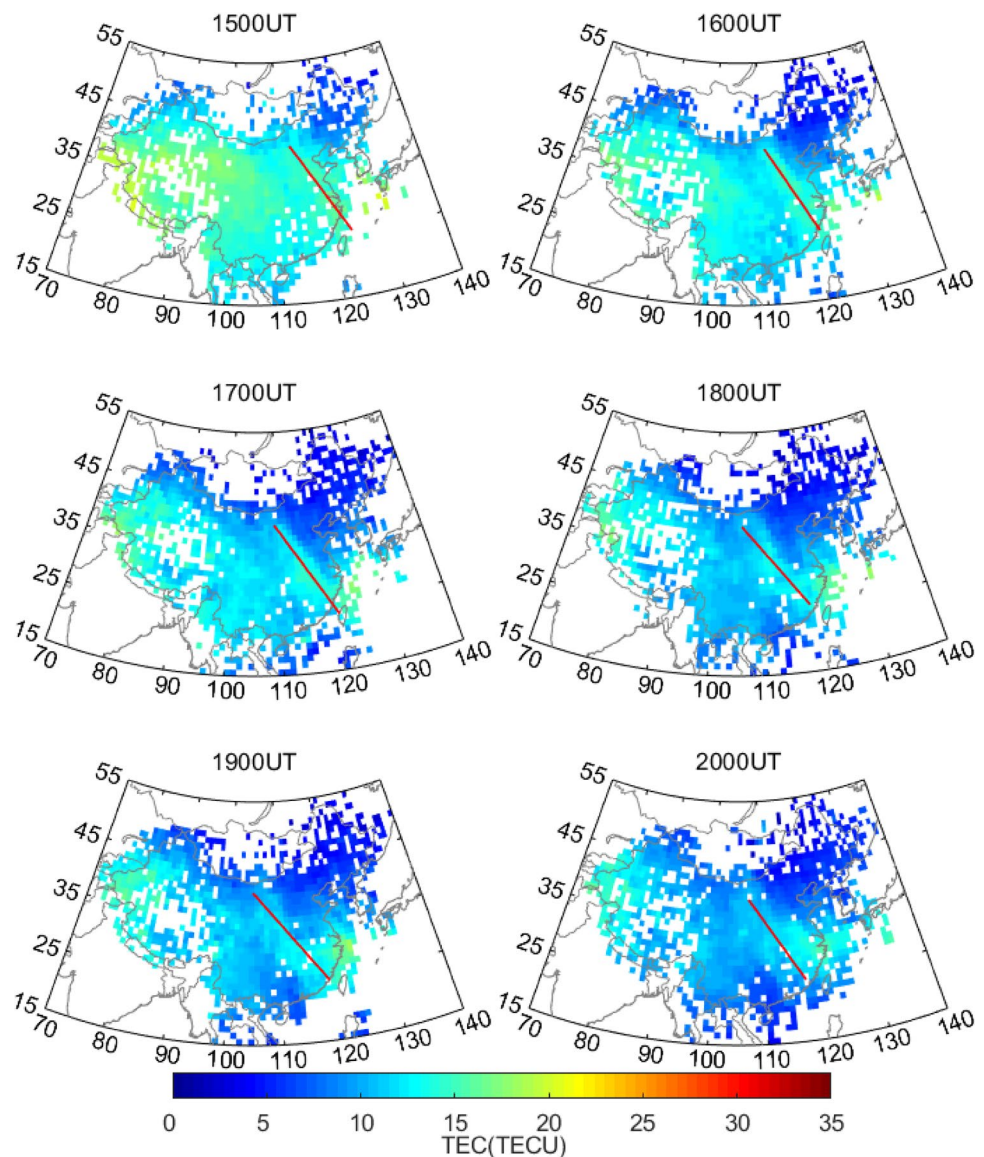
during the recovery phase of the storm will uplift the F layer to higher altitudes where the recombination process is slower, and hence lead to the positive storm response, but afterward the positive storm is disrupted after the second southward turning of the IMF Bz (Mendillo 2006; Lu et al. 2008, 2012; Zou et al. 2013, 2014).

Formation mechanism of the negative storm

The negative ionospheric storm effects at mid-low latitudes were observed by GNSS observations around 00:00–12:00 UT on May 30 (see Fig. 5), which is much later than the recovery phase of the storm. The Ne at different altitudes also decreased significantly in the F region, and the NmF2 reduction is around 75–100% when compared to quiet days (see the bottom row of Fig. 7). It is

typically believed that the negative ionospheric storms are due to thermospheric composition change, more precisely the decreased O/N_2 ratio (e.g., Fuller-Rowell et al. 1994; Astafyeva et al. 2015). The O/N_2 ratio maps from May 27 to May 30 provided by the TIMED/GUVI instrument are shown in Fig. 8. In the Asian sector, the O/N_2 ratios on May 30 were much lower than those during the previous three days, demonstrating that the thermospheric composition change is indeed responsible for the negative storm observed in TEC and EDPs. The O/N_2 ratio does not show a decrease over the Asian sector until May 30, and this also provides a clue for the nearly 20-h duration of the first positive storm observed in this sector. On the other hand, the O/N_2 ratio decrease started early in the American sector on May 28.

Fig. 7 EDPs as a function of altitude and Ne obtained from the COSMIC RO and FY-3C GNOS for different geomagnetic conditions: quiet time (green curves) and storm time (red curves). The small panel at the top-right corner of each subplot represents the satellite tangent point, and the red/blue circles are the location where NmF2 obtained. Green/red curves at each panel represent the quiet/storm time EDPs for almost the same location. Top (**a**, **b**), middle (**c**) and bottom (**d**, **e**) rows in this figure show the EDPs during the first, second positive storm and negative storm, respectively
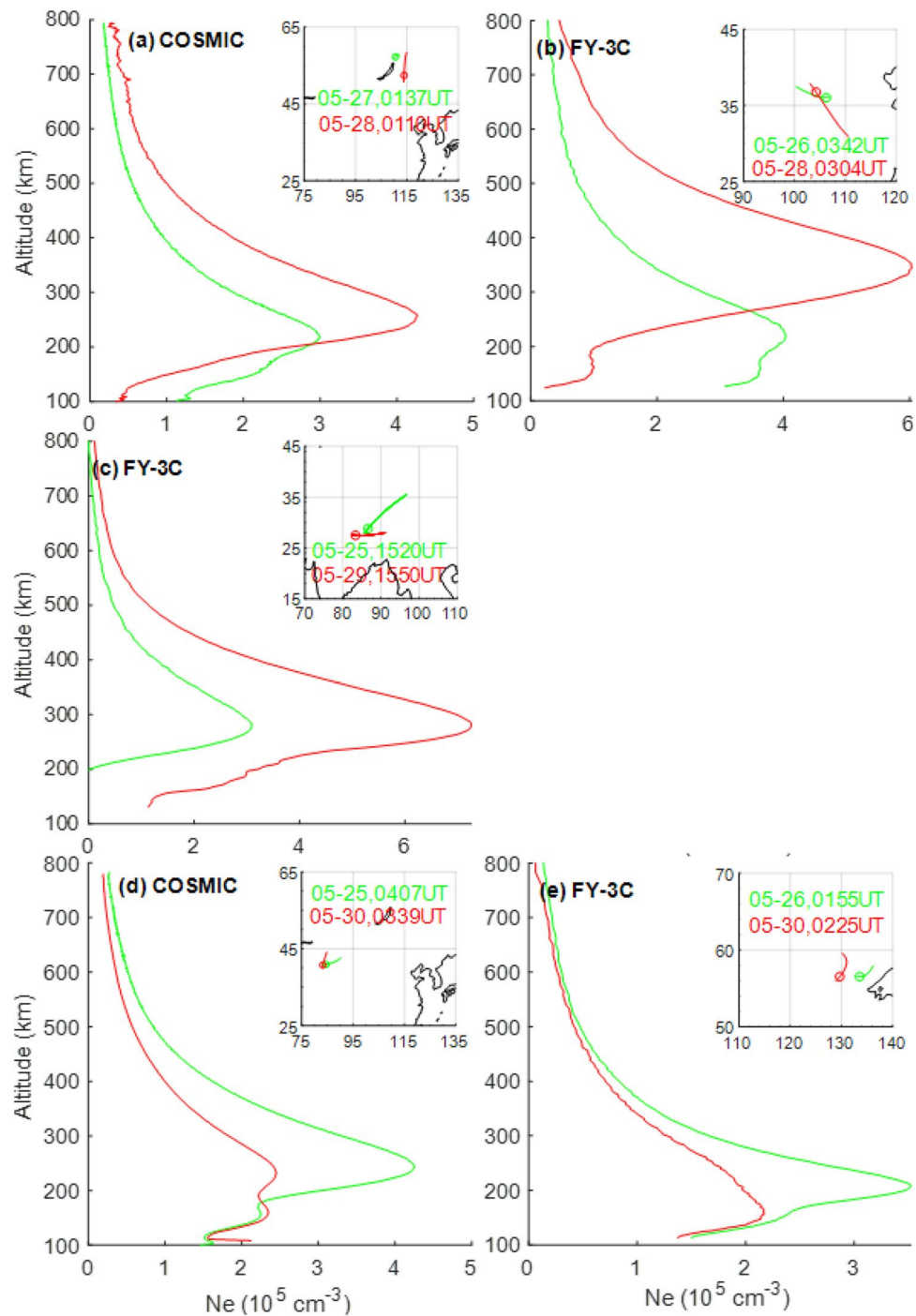
## Formation mechanism of mesoscale TEC enhancement

In Fig. 6, a nighttime band-like TEC enhancement structure aligned in the northwest–southeast direction was detected in the 2D TEC maps at mid-low latitudes (110°–125°E and 20°–40°N) around 15:00–20:00 UT (pre-midnight to the early-morning sector) on May 28. To reveal more detailed information about this band-like TEC enhancement structure, in situ Ne measurements from the Swarm B and DMSP F15&F16 satellites are used when they passed through the Asian sector on May 28. Figure 9 shows the TEC (left) with the available Swarm B and DMSP satellites passes marked by the magenta line, the in situ Ne measurements from the corresponding LEO satellites (middle) and ROTI maps (right). The in situ Ne increased sharply at the locations where the TEC band-like structures are observed. The observed Ne structures resemble the plasma blob

Fig. 8 Thermosphere O/N$_2$ ratio composition maps obtained by the GUVI/TIMED satellite during May 27–30, 2017
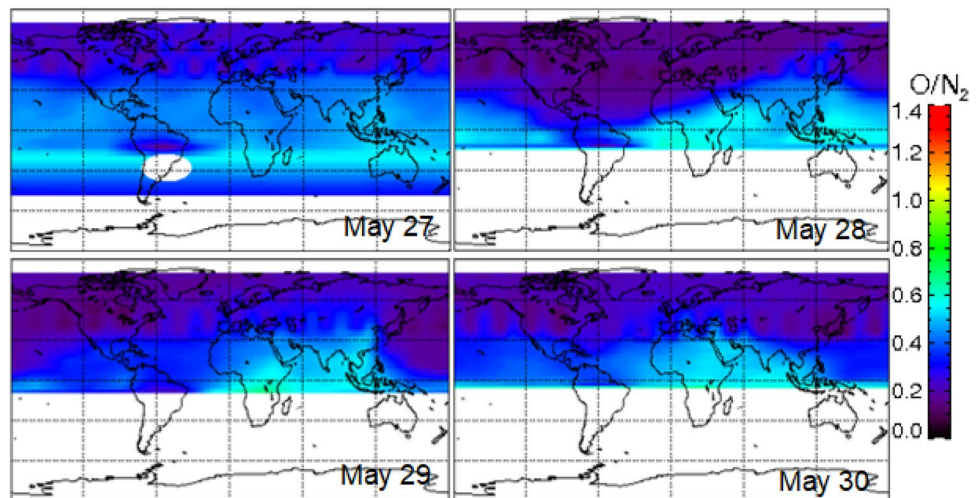
Fig. 9 2D TEC (left) and ROTI (right) maps with superimposed onboard Swarm B and DMSP pass (magenta lines) at the selected time on May 28. In situ electron density (Ne) measurements from Swarm B and DMSP satellites are shown in the middle panels
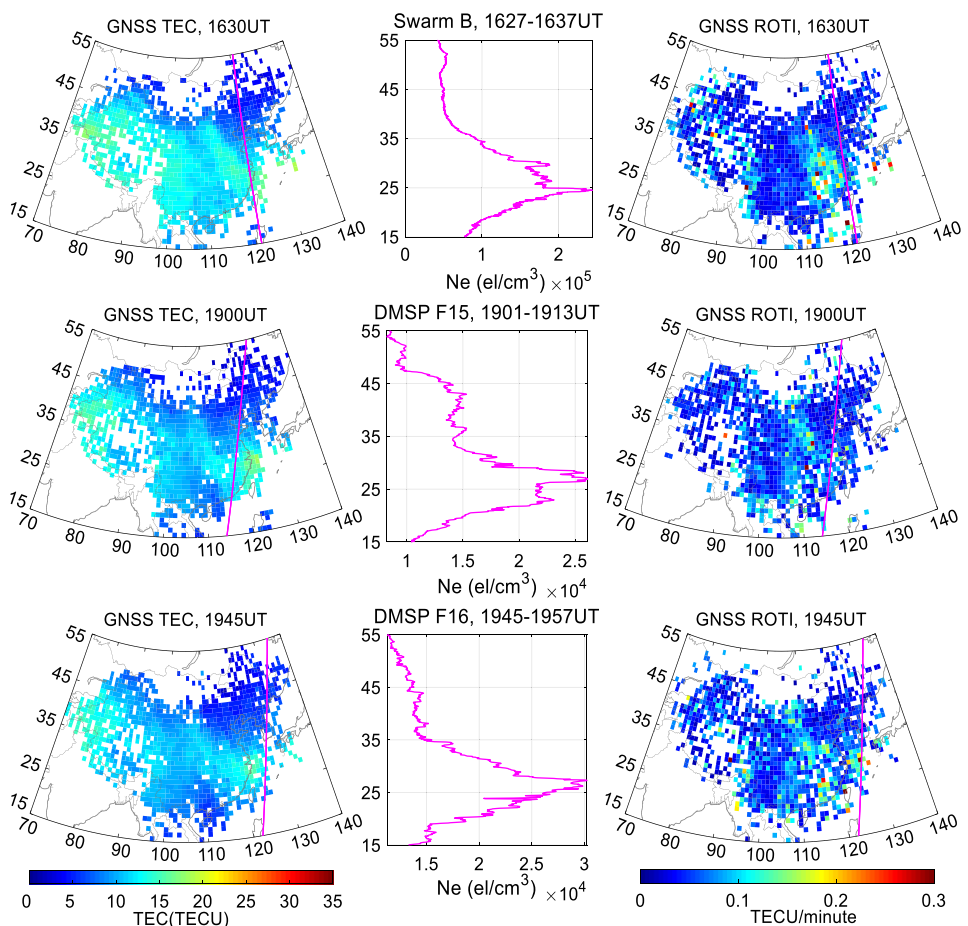
signatures that have been reported earlier (Park et al. 2003; Furno et al. 2008; Huang et al. 2014; Miller et al. 2014; Kil et al. 2019). The combined observations also reveal that the plasma blob structure can actually cover a broad range. The right panels of Fig. 9 show the ROTI map, and one can see that the northwest–southeast aligned TEC structure is collocated well with enhanced ROTI values, suggesting that there are large TEC gradients within the TEC enhancement structure at mid-low latitudes near midnight.

The exact mechanisms of nighttime plasma blob generation and evolution at mid-low latitudes remain a challenge for decades due to a lack of comprehensive observations

of blobs. The current theories associate plasma blobs with either equatorial plasma bubbles (Park et al. 2003; Le et al. 2003; Furno et al. 2008; Huang et al. 2014) or nighttime MSTID (Miller et al. 2014; Kil et al. 2019). In this event study, the 2D structure of the plasma blob is revealed by the 2D TEC map. The TEC enhancement (blob structure) was alignment in the northwest–southeast direction, and it slowly propagated southwestward with a horizontal speed of 90 m/s, which is the averaged speed estimated from every two consecutive 2D TEC maps. It has been reported in many studies that the nighttime MSTID in the northern hemisphere has a wave front elongated from northwest to southeast at nighttime and propagated with speed of 50–250 m/s toward a southwest direction (Saito et al. 2001; Otsuka et al. 2004; Miller et al. 2014). Therefore, the observed plasma blob propagation speed and direction are similar to the typical propagation characteristics of nighttime MSTIDs.

In Fig. 10, the IPP distribution, relative TEC and detrended TEC for PRN20 are presented in the left, middle and right panel, respectively. In the middle panel, the dashed curves are the reference TEC, which are fitted by using a cubic polynomial function, and the solid curves denote the observed TEC time series. The detrended TEC curves in the right panel are obtained by subtracting the reference TEC

from the observed ones. The detrended TEC curves show wave-like signatures from 15:00 to 20:00 UT on May 28, and the amplitude and time durations of these wave-like signatures resemble the TID characteristics. No discernible TEC perturbations can be identified in the quiet time detrended TEC plot on May 26. This nighttime TID is likely generated due to enhanced energy deposition in the auroral latitudes after long-term southward IMF Bz associated with the magnetic cloud. The band-like TEC enhancement structure is associated with the second TID peak, which suggests that the nighttime TID and the blob structure observed in the Ne plot are related.

To further reveal the alignment and propagation of the TID and blob structures, Fig. 11 presents a sequence of 2D detrended TEC maps with a 60-min interval over the Asian sector from 15:00 to 20:00 UT on May 28. The nighttime TID aligned in the northwest–southeast direction appeared first at 15:00 UT (23:00 LT) on May 28, and then gradually propagated southwestward until 18:00 UT (02:00 LT), i.e., from pre-midnight to post-midnight and finally decayed after 19:00 UT (03:00 LT). The spatial structure, propagation trend and temporal evolution of the nighttime TID detected, in this case, resemble typical nighttime MSTIDs (Saito et al. 2001; Otsuka et al. 2004; Miller et al. 2014; Kil et al. 2019).
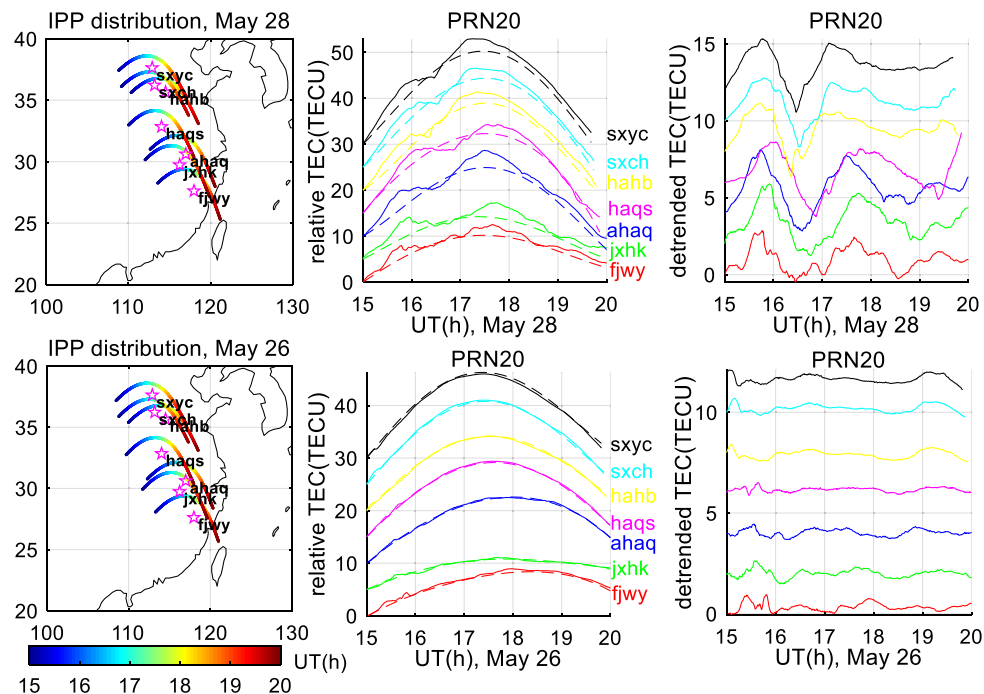

Fig. 10 IPP trajectories and GNSS receiver locations (left), relative TEC (middle) and detrended TEC (right) time series for GPS satellite PRN20 during 15:00–20:00 UT on May 28 (disturbed day) and 26 (quiet day). Magenta stars in the left panel represent seven GNSS station locations. Solid and dashed curves in the middle panel are the observed TEC and reference TEC, respectively. Dashed curves are regarded as reference TEC value, which is fitted by using the cubic polynomial function. Detrended TEC time series in the right panel is the difference by using the observed TEC minus reference TEC. Relative TEC or detrended TEC time series is plotted from high to low latitudes by shifting several TECU in middle and right panels. Seven GNSS stations (fjwy, jxhk, ahaq, haqs, hahb, sxch and sxyc) are marked by different colors near the corresponding curves

Fig. 11 2D detrended TEC maps with one-hour interval from 15:00 to 20:00 UT on May 28 used to show nighttime TID-like signatures over the Asian sector. Full sets of 2D TEC detrended maps with a 10-min interval are available in Movie 5 of the supporting information
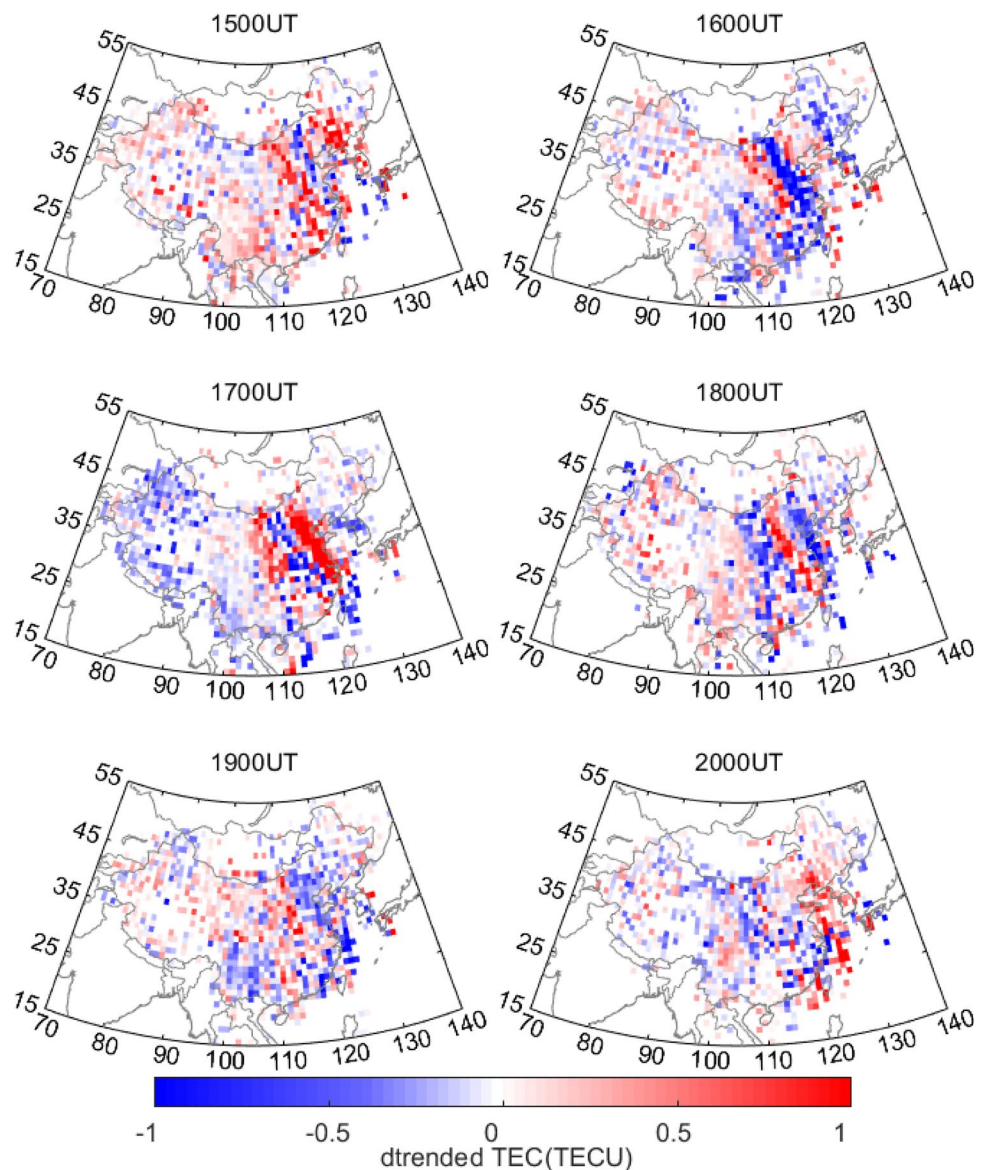
Together with the blob signature detected by the Swarm B and DMSP F15&F16 in situ Ne measurements, we suggest that the nighttime MSTID and blob are manifestations of the same ionospheric mesoscale structure with different plasma characteristics revealed by different measurement techniques.

We now further discuss how plasma blobs are associated with nighttime TIDs at mid-low latitudes. The nighttime TID is typically understood as a manifestation of atmospheric gravity waves (AGWs) excited due to enhanced auroral energy deposition or polarization electric field near midnight (Saito et al. 2001; Otsuka et al. 2004). It is usually observed to propagate southwestward from auroral latitudes to mid and low latitudes. The TID-blob connection is suggested as follows: when the nighttime TID grows, the plasma blobs start to appear near the locations of the TID and extend to southwestward direction driven by the TID (Miller et al. 2014; Kil et al. 2019). In Miller et al. (2014), a group of blobs was detected by the C/NOFS Ni measurements when nighttime electrified MSTID propagated southwestward, and the authors suggested that the observed blobs may be the signature of the MSTIDs in the topside ionosphere. Recent work by Kil et al. (2015, 2019) revealed the detection of MSTID near the locations of the plasma blobs in the absence of equatorial plasma bubbles, supporting the TID-blob association well. The multi-instrument observations reported in this event further support that the nighttime TIDs are plausible sources of plasma blobs.

Summary and conclusions

We investigated multi-scale ionospheric responses to the May 27, 2017, intense geomagnetic storm over the Asian sector by using multi-instrumental observations, including GNSS TEC and other complementary datasets.

(1) Two ionospheric positive storm periods were observed. The first one was observed in the noon–afternoon sector during the main phase of the storm on May 28, with the maximum TEC increment over 120%. It lasted for more than 20 h, the same as the long duration southward IMF Bz of the CME magnetic cloud. The considerable increases in both NmF2 and hmF2 observed by the COSMIC RO and FY-3C GNOS EDPs suggest that the first positive storm was due to the upward lifting of the *F* layer with reduced loss and continued solar production. The second positive storm was of a smaller scale and occurred on the nightside during the recovery phase of the storm on May 29. We suggest that the second positive phase is likely part of the nighttime EIA crest and formed due to the DDEF during the recovery phase of the storm and disrupted due to the westward PPEF induced by the second southward turning of the IMF Bz.

(2) A negative storm occurred from 00:00 to 12:00 UT on May 30 over the Asian sector nearly 2 days after the main phase, with the most severe TEC decrease reaching 10 TECU below 30°N at 120°E around 06:00 UT. The great electron density reduction observed in the COSMIC RO and FY-3C GNOS EDPs also confirmed this negative ionosphere storm. The decreased O/N_2 ratio from TIMED/GUVI measurements on May 30 demonstrated that the thermospheric composition change was responsible for the negative storm.

(3) A band-like TEC structure was observed aligning in the northwest–southeast direction at mid-low latitudes (110°–125°E and 20°–40°N) and propagated slowly southwestward between 23:00 and 04:00 LT on May 28 during the recovery phase of the storm. The spatial structure, propagation trend and temporal evolution of the TEC structure are consistent with the nighttime MSTID. The in situ Ne observations from the Swarm B and DMSP F15&16 satellites revealed that the density enhancement resembled the so-called plasma blob. Therefore, these multi-instrument observations of TID and blob suggest that the plasma blobs can be the topside ionosphere manifestation of TID peaks, which are consistent with the TID-blob theory proposed before.

References

Aa E, Huang W, Liu S, Ridley A, Zou S, Shi L, Wang T (2018) Midlatitude plasma bubbles over China and adjacent areas during a magnetic storm on 8 September 2017. Space Weather 16(3):321–331

Abadi P, Otsuka Y, Tsugawa T (2015) Effects of pre-reversal enhancement of E×B drift on the latitudinal extension of plasma bubble in Southeast Asia. Earth Planets Space 67(1):74

Abdu MA (2012) Equatorial spread F/plasma bubble irregularities under storm time disturbance electric fields. J Atmos Terr Phys 75:44–56. https://doi.org/10.1016/j.jastp.2011.04.024

Abdu MA, Maruyama T, Batista IS, Saito S, Nakamura M (2007) Ionospheric responses to the October 2003 superstorm: longitude/local time effects over equatorial low and middle latitudes. J Geophys Res 112:A10306. https://doi.org/10.1029/2006JA012228

Astafyeva E, Zakharenkova I, Förster M (2015) Ionospheric response to the 2015 St. Patrick's Day storm: a global multi-instrumental overview. J Geophys Res Space Phys 120:9023–9037. https://doi.org/10.1002/2015JA021629

Astafyeva E, Zakharenkova I, Huba JD, Doornbos E, Van den IJssel J (2017) Global ionospheric and thermospheric effects of the June 2015 geomagnetic disturbances: multi-instrumental observations and modeling. J Geophys Res Space Phys 122(11):11–716

Astafyeva E, Zakharenkova I, Hozumi K, Alken P, Coïsson P, Hairston MR, Coley WR (2018) Study of the equatorial and low-latitude electrodynamic and ionospheric disturbances during the 22–23 June 2015 geomagnetic storm using ground-based and spaceborne techniques. J Geophys Res Space Phys 123(3):2424–2440

Cherniak I, Zakharenkova I (2016) First observations of super plasma bubbles in Europe. Geophys Res Lett 43(21):11–137

Cherniak I, Krankowski A, Zakharenkova I (2018) ROTI maps: a new IGS ionospheric product characterizing the ionospheric irregularities occurrence. GPS Sol 22(3):69

Choi H-S, Kil H, Kwak Y-S, Park Y-D, Cho K-S (2012) Comparison of the bubble and blob distributions during the solar minimum. J Geophys Res 117:A04314. https://doi.org/10.1029/2011JA017292

Christensen AB et al (2003) Initial observations with the global ultraviolet imager (GUVI) on the NASA TIMED satellite mission. J Geophys Res 108(A12):1451. https://doi.org/10.1029/2003JA009918

Crowley G et al (2006) Global thermosphere-ionosphere response to onset of 20 November 2003 storm. J Geophys Res 111:A10S18. https://doi.org/10.1029/2005JA011518

Danilov AD (2013) Ionospheric F-region response to geomagnetic disturbances. Adv Space Res 52(3):343–366

Fuller-Rowell TJ, Codrescu MV, Moffett RJ, Quegan S (1994) Response of the thermosphere and ionosphere to geomagnetic storms. J Geophys Res 99:3893–3914. https://doi.org/10.1029/93JA02015

Furno I et al (2008) Experimental observation of the blob-generation mechanism from interchange waves in a plasma. Phys Rev Lett 100(5):055004

Garcia FJ, Kelley MC, Makela JJ, Huang CS (2000) Airglow observations of mesoscale low-velocity traveling ionospheric disturbances at midlatitudes. J Geophys Res Space Phys 105(A8):18407–18415

Haaser RA, Earle GD, Heelis RA, Klenzing J, Stoneback R, Coley WR, Burrell AG (2012) Characteristics of low-latitude ionospheric depletions and enhancements during solar minimum. J Geophys Res 117:A10305. https://doi.org/10.1029/2012JA017814

Heelis RA, Sojka JJ, David M, Schunk RW (2009) Storm time density enhancements in the middle-latitude dayside ionosphere. J Geophys Res 114:A03315. https://doi.org/10.1029/2008JA013690

Huang C-S, Foster JC, Kelley MC (2005) Long-duration penetration of the interplanetary electric field to the low-latitude ionosphere during the main phase of magnetic storms. J Geophys Res. https://doi.org/10.1029/2005JA011202

Huang C-S, Le G, de La Beaujardiere O, Roddy PA, Hunton DE, Pfaff RF, Hairston MR (2014) Relationship between plasma bubbles and density enhancements: observations and interpretation. J Geophys Res Space Phys 119:1325–1336. https://doi.org/10.1002/2013JA019579

Jin R, Jin S, Feng G (2012) M_DCB: Matlab code for estimating GNSS satellite and receiver differential code biases. GPS Sol 16(4):541–548

Kil H, Paxton LJ (2017) Global distribution of nighttime medium-scale traveling ionospheric disturbances seen by swarm satellites. Geophys Res Lett 44(18):9176–9182

Kil H, Kwak YS, Lee WK, Miller ES, Oh SJ, Choi HS (2015) The causal relationship between plasma bubbles and blobs in the low-latitude F region during a solar minimum. J Geophys Res Space Phys 120(5):3961–3969

Kil H, Paxton LJ, Jee G, Nikoukar R (2019) Plasma blobs associated with medium-scale traveling ionospheric disturbances. Geophys Res Lett 46(7):3575–3581

Le G, Huang CS, Pfaff RF, Su SY, Yeh HC, Heelis RA, Hairston M (2003) Plasma density enhancements associated with equatorial spread F: ROCSAT-1 and DMSP observations. J Geophys Res Space Phys 108(A8):1318. https://doi.org/10.1029/2002JA009592

Lei J et al (2007) Comparison of COSMIC ionospheric measurements with ground-based observations and model predictions: preliminary results. J Geophys Res 112:A07308. https://doi.org/10.1029/2006JA012240

Lu G, Goncharenko LP, Richmond AD, Roble RG, Aponte N (2008) A dayside ionospheric positive storm phase driven by neutral winds. J Geophys Res 113:A08304. https://doi.org/10.1029/2007JA012895

Lu G, Goncharenko L, Nicolls MJ, Maute A, Coster A, Paxton LJ (2012) Ionospheric and thermospheric variations associated with prompt penetration electric fields. J Geophys Res 117:A08312. https://doi.org/10.1029/2012JA017769

Mannucci AJ et al (2005) Dayside global ionospheric response to the major interplanetary events of October 29–30, 2003 "Halloween Storms". Geophys Res Lett 32:L12S02. https://doi.org/10.1029/2004GL021467

Mendillo M (2006) Storms in the ionosphere: patterns and processes for total electron content. Rev Geophys 44:RG4001. https://doi.org/10.1029/2005RG000193

Miller ES, Kil H, Makela JJ, Heelis RA, Talaat ER, Gross A (2014) Topside signature of medium-scale traveling ionospheric disturbances. Ann Geophys 32(8):959–965. https://doi.org/10.5194/angeo-32-959-2014

Nava B et al (2016) Middle-and low-latitude ionosphere response to 2015 St. Patrick's Day geomagnetic storm. J Geophys Res Space Phys 121:3421–3438. https://doi.org/10.1002/2015JA022299

Otsuka Y, Shiokawa K, Ogawa T, Wilkinson P (2004) Geomagnetic conjugate observations of medium-scale traveling ionospheric disturbances at midlatitude using all-sky airglow imagers. Geophys Res Lett 31:L15803. https://doi.org/10.1029/2004GL020262

Park J, Min KW, Lee J-J, Kil H, Kim VP, Kim H-J, Lee E, Dae Young Lee DY (2003) Plasma blob events observed by KOMPSAT-1 and DMSP F15 in the low latitude nighttime upper ionosphere. Geophys Res Lett 30(21):2114. https://doi.org/10.1029/2003GL018249

Pi X, Mannucci A, Lindqwister UJ, Ho CM (1997) Monitoring of global ionospheric irregularities using the worldwide GPS network. Geophys Res Lett 24(18):2283–2286

Saito A et al (2001) Traveling ionospheric disturbances detected in the FRONT campaign. Geophys Res Lett 28(4):689–692. https://doi.org/10.1029/2000GL011884

Singh R, Sripathi S (2017) Ionospheric response to 22–23 June 2015 storm as investigated using ground-based ionosondes and GPS receivers over India. J Geophys Res Space Phys 122(11):11–645

Sripathi S, Sreekumar S, Banola S, Emperumal K, Tiwari P, Kumar BS (2015) Low-latitude ionosphere response to super geomagnetic storm of 17/18 March 2015: results from a chain of ground-based observations over Indian sector. J Geophys Res Space Phys 120(12):10–864

Tsugawa T, Otsuka Y, Coster AJ, Saito A (2007) Medium-scale traveling ionospheric disturbances detected with dense and wide TEC maps over North America. Geophys Res Lett 34:L22101. https://doi.org/10.1029/2007GL031663

Yao Y, Liu L, Kong J, Zhai C (2016) Analysis of the global ionospheric disturbances of the March 2015 great storm. J Geophys Res 121(12):12157–12170

Yao Y, Liu L, Kong J, Zhai C (2018) Global ionospheric modeling based on multi-GNSS, satellite altimetry, and Formosat-3/COSMIC data. GPS Solut 22(4):104

Zou S, Ridley AJ, Moldwin MB, Nicolls MJ, Coster AJ, Thomas EG, Ruohoniemi JM (2013) Multi-instrument observations of SED during 24–25 October 2011 storm: implications for SED formation processes. J Geophys Res 118:7798–7809. https://doi.org/10.1002/2013JA018860

Zou S, Moldwin MB, Ridley AJ, Nicolls MJ, Coster AJ, Thomas EG, Ruohoniemi JM (2014) On the generation/decay of the storm-enhanced density (SED) plumes: role of the convection flow and field-aligned ion flow. J Geophys Res 119:543–8559. https://doi.org/10.1002/2014JA020408

Publisher's Note Springer Nature remains neutral with regard to jurisdictional claims in published maps and institutional affiliations.

Lei Liu is a Ph.D. student at Wuhan University, China. He is currently a visiting Ph.D. student in Dr. S. Zou's group at the University of Michigan, Ann Arbor. He received his master's degree in Geodesy and Geomatics in 2017 at Wuhan University. His research interests include GNSS ionosphere model and space weather monitoring.

Yibin Yao is currently a Professor at the School of Geodesy and Geomatics, Wuhan University, China. He obtained his Ph.D. in Geodesy and Surveying Engineering from Wuhan University in 2004. His current research interests include GNSS ionospheric/atmospheric/meteorological studies and high-precision GNSS data processing.
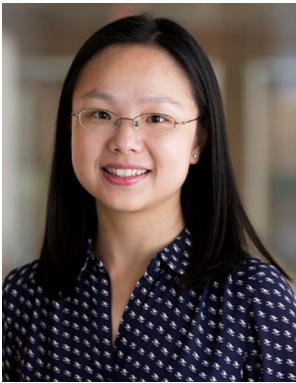
Shasha Zou is an associate professor at the University of Michigan, Ann Arbor. She got her B.S. degree in Space Physics from the University of Science and Technology of China (USTC) in 2004, and received her Ph.D. degree in Space Physics from the University of California, Los Angeles (UCLA) in 2009. Dr. Zou's research focuses on understanding the dynamic coupling between the Earth's magnetosphere, ionosphere and thermosphere during geomagnetic disturbances, and the resultant space weather impact. She has extensive experience in analyzing and interpreting observations obtained by various ground-based and space-based instruments, as well as results from numerical modeling.
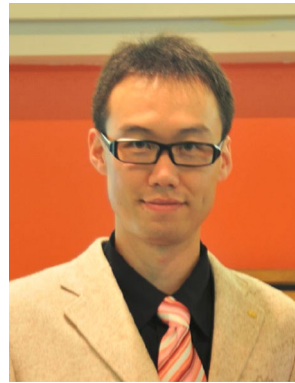
Ercha Aa is an associate research scientist at the National Space Science Center, Chinese Academy of Sciences. He received his B.S. in electrical engineering from Wuhan University in 2007. He received his Ph.D. degree in space physics from Peking University in 2012. His current interests focused on space weather and its impact, equatorial plasma irregularities, ionospheric modeling, and data assimilation.